Telluride-Based Atomically Thin Layers of Ternary Two-Dimensional Transition Metal Dichalcogenide Alloys

Amey Apte,[†] Aravind Krishnamoorthy,[‡] Jordan Adam Hachtel,[§] Sandhya Susarla,[†]
Juan Carlos Idrobo,[§] Aiichiro Nakano,[‡] Rajiv K. Kalia,[‡] Priya Vashishta,*,[‡]
Chandra Sekhar Tiwary,*,[†,∥] and Pulickel M. Ajayan*,[†]

[†]Department of Materials Science & NanoEngineering, Rice University, 6100 Main Street, Houston, Texas 77005, United States

[‡]Collaboratory for Advanced Computing and Simulations, Department of Physics and Astronomy, University of Southern California, Los Angeles, California 90089, United States

[§]Center for Nanophase Materials Science, Oak Ridge National Laboratory, Oak Ridge, Tennessee 37831, United States

[∥]Metallurgical and Materials Engineering, Indian Institute of Technology, Kharagpur 721302, West Bengal, India

S *Supporting Information*

ABSTRACT: Alloying in two-dimensional (2D) transition metal dichalcogenides (TMDCs) has allowed band gap engineering and phase transformation, as well as modulation of electronic properties. However, most of the efforts have been focused on alloying between transition metal cations. Among those that emphasize alloying between chalcogenide anions, the sulfide–selenide combinations are popular with a few reports on selenide–telluride combinations. In this work, we show a facile chemical vapor deposition method to obtain stable alloying between selenide and telluride anions in monolayer Mo-$Se_{2(1-x)}Te_{2x}$ alloy. These alloys retain the monolayer 2H symmetry and show good photoluminescence and band gap tunability in the near-infrared region. The nature and percentage of alloying is further confirmed and quantified via AFM, XPS, and HAADF-STEM imaging and polarized Raman spectroscopy. The stability of the two chalcogens in the monolayer 2H lattice is also consistent with thermodynamic phase mixing via DFT simulations. The work demonstrates a straightforward method of synthesizing telluride-based 2D TMDC alloys for further studies and emerging applications.
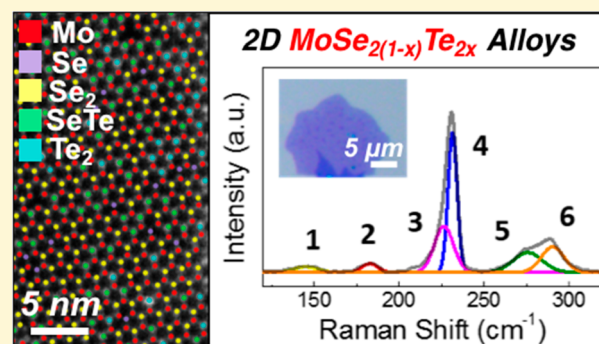
Layered two-dimensional (2D) transitional metal dichalcogenides (TMDCs) are MX_2-type compounds (M = Mo, W; X = S, Se, Te) with hexagonal symmetry and strong bonding in the "*ab*" in-plane directions and weak van der Waals' interactions in the out-of-plane "*c*" direction.[1−9] While the single-phase TMDCs have been extensively studied over past years, exploring alloying in such TMDC materials has recently gained momentum with aims of improving stability via increasing entropy, improving band gap tunability and engineering, applications in valleytronics, studying structural phase transformations, and emergent magnetism.[10−19] It has also been reported that substitutional doping is the energetically preferred route over occupying the interstitial locations in these atomically thin systems.[20,21] Both p- and n-type dopants such as Nb, and Mn, Re, and so on, were explored at M sites.[22−26] While most of the substitutional doping experiments have been carried out on the "M" (transition metal) site, there are some reports of doping at the "X" (chalcogen) site as well.[10,27,28] Recently, the telluride-based TMDCs have been gaining more interest than sulfide- and selenide-based TMDCs, mostly due to the rich variety of structural phases (2H, 1T, and 1T′), for which the

corresponding compounds, such as $MoTe_2$, WTe_2, and so on, are stable at room temperature, as well as the interesting physics these phases offer for study.[29−31] While the 2H phase is semiconducting, the 1T/1T′ phases are semi-metallic or metallic, and support greater electronic mobility as well as exotic features such as topological states.[32−37] Therefore, the interest in telluride-based TMDCs has exploded with studies focusing on applications such as atomically thin metal–semiconductor contacts from two phases of the same material.[38,39] 2H−1T′ structural phase transitions in such TMDCs have been recently reported—both occurring within the same material as well as in alloys: Wang et al. observed the transformation in monolayer $MoTe_2$ by electrostatic doping, whereas Zhang et al. and Yu et al. observed similar transitions in the case of $W_{1-x}Mo_xTe_2$ and $WSe_{2(1-x)}Te_{2x}$ ternary alloys.[28,40] However, such studies are either limited to density functional theory (DFT) calculations or bulk sample synthesis via chemical

vapor transport and few-layer growth initiated by predeposition of precursors via intricate techniques such as high-vacuum electron beam assisted deposition. Diaz et al. recently reported synthesis and ARPES studies of $MoSe_2$ and $MoSe_{2(1-x)}Te_{2x}$ solid solutions grown by molecular beam epitaxy (MBE) on epitaxial and highly crystalline HOPG and MoS_2 substrates.[41] While the focus of their study was more on understanding the valence band structure of $MoSe_2$ on the two substrates and how doping with Te results in mostly similar (i.e., isoelectronic) structure, they have not provided insight into the atomistic nature of the alloying (e.g., high-angle annular dark field−scanning transmission electron microscopy (HAADF-STEM)) which is important for such 2D materials. Recent effort on this aspect was reported by Lin et al. by a heavily STEM-focused study of the 2D $MX_{2x}Te_{2(1-x)}$ alloys exfoliated from bulk single crystals.[42] They found anisotropic chalcogen bond ordering in the 1T′-type alloys, whereas the 2H-type were isotropic. However, in their case, the other characterizations of such alloy samples, which are equally if not more, important, were not reported.

In this work, we provide an inclusive report of the bottom-up synthesis of monolayer $MoSe_{2(1-x)}Te_{2x}$ alloys via a relatively facile method of chemical vapor deposition (CVD) and their comprehensive characterization via multiple techniques: the ratio of tellurium and selenium precursors was varied to incorporate progressive amounts of tellurium in the $MoSe_2$ lattice. The structural and chemical nature of the samples was extensively characterized using Raman and photoluminescence spectroscopy as well as X-ray photoelectron spectroscopy (XPS); increasing amounts of tellurium induces a red shift in the optical band gap from 1.55 eV for pure $MoSe_2$ up to 1.3 eV for the alloyed samples. This change is reflected in the corresponding Raman spectra as well. XPS spectra show slight reduction in binding energies of molybdenum atoms, indicative of a change in their chemical coordination. Detailed variations in morphology were observed using optical microscopy and atomic force microscopy, whereas the crystal structure examination via high-resolution scanning transmission electron microscopy revealed complete alloying of Se and Te at chalcogen sites in the monolayer 2H phase. This observation is also supported by thermodynamic analysis of phase mixing and phase separation in $MoSe_{2(1-x)}Te_{2x}$ crystals using ab initio DFT and empirical molecular dynamics simulations (MD) with classical force fields. Polarized Raman spectra and peak deconvolution helped to show the differences in the symmetric and nonsymmetric vibrational modes, further confirming the alloying process in the 2H phase.

Figure 1a shows the schematic of the synthesis/growth process as discussed in Experimental Details. This was followed by the preliminary identification and characterization of the samples. The 275 nm SiO_2 layer on top of the Si substrates helps in delivering good contrast and aid identification of the 2D flakes and changes in morphology. The gradual changes in the Raman and PL spectra along with varying Se/Te content have been plotted in Figure 1b,c, respectively. Starting with the pure $MoSe_2$ sample, there are sharp triangular edges with a generally large enough average size of 50 μm. The Raman and PL spectra (red curve) show the characteristic strong A_{1g} mode at 239 cm^{-1} and emission at 1.55 eV. For alloy A (grown with precursor Se:Te ratio of 1:1), the 2D flakes preserve the hexagonal shape and symmetry; however, their average size decreases to 20−30 μm. The Raman spectrum (green curve) shows a slight red shift of the A_{1g} mode to 237 cm^{-1}, whereas the PL emission undergoes a more noticeable red shift to 1.49 eV. For the next sample (grown
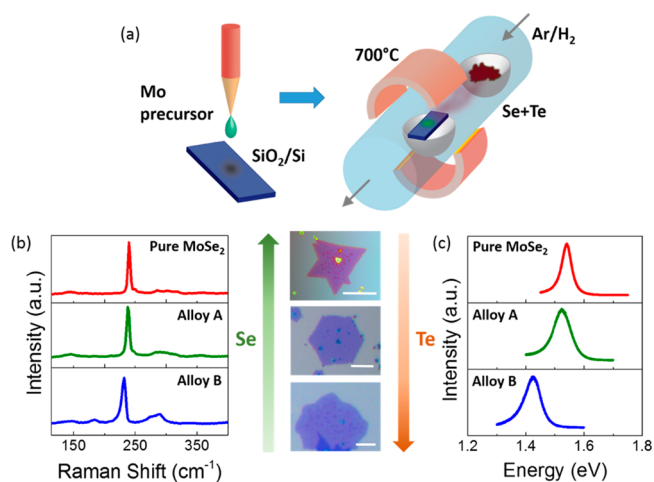

Figure 1. Synthesis strategy of $MoSe_{2(1-x)}Te_{2x}$ monolayers: (a) Schematic of CVD growth of Te-doped $MoSe_2$ monolayers. (b) Raman spectra of Pure $MoSe_2$ and the Te-doped alloy samples. The increasing Te content is depicted alongside with changing morphologies of the monolayer flakes from optical micrographs (scale bars = 50 μm, 10 μm, and 5 μm from top to bottom). (c) Photoluminescence spectra of the three samples analogous to the Raman spectra showing tunable emission characteristics from the visible to the near-infrared.

with substantially increased Se:Te ratio 1:5), i.e., alloy B, the change in 2D morphology is visible with a lack of sharp facets to the flakes. Our CVD technique of growing these alloys yields larger flake sizes important for further studies and applications compared to reported methods (e.g., STM image in Figure 3e of Diaz et al. showing fragmented polycrystalline grains even at sub-micrometer lengths)[41] The Raman spectrum (blue curve) features a relatively broad and asymmetric peak centered roughly at 231 cm^{-1} (deconvolution discussed later). The increased presence of Te atoms also red shifts the PL emission of alloy B to 1.42 eV. Thus, the Raman and PL spectra show consistent red-shifting of the prominent features borne out of increasing tellurium content.

Further analysis of the samples was carried out by atomic force microscopy (AFM) and X-ray photoelectron spectroscopy (XPS). AFM helps understand the detailed variation in morphology at a resolution beyond the grasp of conventional optical imaging as well as confirm the thicknesses of layered materials; XPS sheds light on the chemical bonding and valence states of various atoms in a compound with nanometer-level probing. Panels a−c of Figure 2 show the AFM and XPS results of pure $MoSe_2$ and alloys A and B, respectively. In Figure 2a, the AFM image and line profile of pure $MoSe_2$ indicate monolayer thickness (∼0.8 nm) and tiny secondary growth at the edges and near the center, which is a common signature of lateral edge termination and epitaxial growth, respectively. For alloy A, we observe a similar sharp edge and monolayer thickness. Following the AFM images, we come to the XPS analysis. For all spectra, the binding energies were referenced by the adventitious carbon 1s peak at 284.8 eV (not shown). In panel a, the elemental spectra for the Mo 3d and Se 3d regions of pure $MoSe_2$ are shown. The Mo $3d_{5/2}$ and $3d_{3/2}$ peaks at binding energies 229.2 and 232.4 eV indicate a Mo^{4+} valence state and have been reported for the 2H phase; the corresponding Se $3d_{5/2}$ and $3d_{3/2}$ peaks occur at 54.7 and 55.5 eV, respectively, indicating the Se^{2-} state. For the alloy samples, the Te 3d region is included to analyze the tellurium composition. In Figure 2b, alloy A shows slight shifts in the Mo 3d and Se 3d binding energies (229.4 eV,
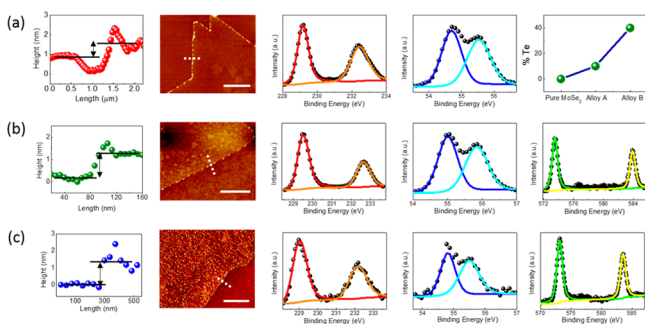
Figure 2. Atomic force microscopy (AFM) and X-ray photoelectron spectroscopy (XPS) data: (a) pure MoSe$_2$, (b) alloy A, and (c) alloy B, respectively (AFM image scale bars: 10, 0.5, and 1 μm from top to bottom). The AFM line profiles show thickness consistent with monolayers with alloy C showing multilayer growth. The XPS spectra show Mo 3d, Se 3d, and Te 3d elemental regions, respectively. The last image in row a depicts the trend of increasing relative telluride concentration in the samples as calculated from XPS data.
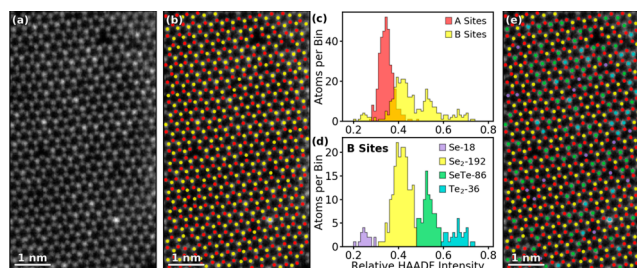

Figure 3. High-angle annular dark field (HAADF) imaging: (a) monolayer region of alloy sample observed in a scanning transmission electron microscope (STEM). Region shows the 2H phase of the alloy with significant changes in contrast in the monolayer. (b) Atoms sorted in to A Sites (red) and B Sites (yellow) by atomic coordination. (c) Histogram of HAADF intensities showing that all alloying occurs on the B sites while the A site contrast is highly uniform. (d) B site intensity histogram labeling the separate peaks by their respective Z-contrasts. (e) Atom labeled image demonstrating successful chalcogenide alloying in the MoSe$_{2(1-x)}$Te$_{2x}$ samples.

232.6 eV and 54.9 eV, 55.8 eV). The Te 3d$_{5/2}$ and 3d$_{3/2}$ peaks occur at 573.5 and 583.8 eV, respectively, indicating that tellurium atoms are in the Te^{2-} state. The relative concentration of Te in alloy A derived from XPS turns out to be ~10% (i.e., $x \approx$ 0.1; calculations are given in the Supporting Information (SI)). The minute yet important change in the XPS binding energies (BEs) can be seen in the spectra for alloy B in Figure 2c. The Mo 3d peaks display a downshift to 228.9 and 232.1 eV, whereas the Se 3d peaks occur at 54.7 and 55.4 eV, respectively. This downshift in Mo^{4+} BE is expected as tellurium is less electronegative than selenium and in agreement with other reports. The corresponding Te 3d peaks occur at 573.1 and 583.5 eV. The relative tellurium concentration in alloy B comes out to be ~40% (i.e., $x \approx$ 0.28). The trend of increasing tellurium concentration in the four samples is plotted in the last position in the row of Figure 2a. Moreover, the obtained x values are in good agreement with the band gaps obtained via photoluminescence (PL) emission in Figure 1c via the band-bowing formula given by Kang et al.[19]

$$E_g^{alloy} = xE_g^1 + (1-x)E_g^2 - bx(1-x)$$

Here, b is the band-bowing parameter with a value of 0.12 calculated for MoSe$_{2(1-x)}$Te$_{2x}$ in the aforementioned reference. Given the band gaps of monolayer MoSe$_2$ (E_g^1) and (2H) MoTe$_2$ (E_g^2) are 1.55 and 1.1 eV respectively, we find that E_g^{alloy} for alloys A ($x \approx$ 0.1) and B ($x \approx$ 0.28) come out to be ~1.49 eV and ~1.4 eV, which agree well within experimental limits with the values inferred from Figure 1c.

To observe the chalcogenide alloying directly, the samples were examined with atomic-resolution scanning transmission electron microscopy. A high-angle annular dark field image of a monolayer region of the MoSe$_{2(1-x)}$Te$_{2x}$ alloy is shown in Figure 3a, which exhibits significant site-to-site contrast variations. HAADF images are formed through Z-contrast (especially in monolayer materials), where the HAADF intensity is roughly proportional to the square atomic number of the atom/atomic columns. Thus, the atomistic nature of the alloying in the monolayer can be determined by examining the HAADF intensities of the different atomic sites. First, the monolayer is sorted into A sites and B sites by the atomic coordination of each atom in the HAADF image (sorted image shown in Figure 3b). The HAADF intensities of both sites are then plotted in a histogram in Figure 3c.

From the histograms, it can be seen that A site intensity is highly uniform across the monolayer, while the B sites show four distinct peaks in the HAADF intensity histogram, indicating that the A sites are the metal Mo sites and the B sites are the Se/Te chalcogenide sites. The composition of each peak in the histogram can be determined by examining the atomic numbers (and effective atomic numbers) of the constituent atom: Z(Se) = 34, Z(Mo) = 42, Z_{eff}(Se$_2$) = 48.1, Z(Te) = 52, Z_{eff}(SeTe) = 62.1, and Z_{eff}(Te$_2$) = 73.5. The Z-contrasts match remarkably well to the peaks in the relative HAADF intensity histogram shown in Figure 3c, with the lowest HAADF intensity peak in the B sites corresponding to a single Se atom, the second corresponding to an Se$_2$ column, the third corresponding to an intermixed Se/Te column, and the final high HAADF intensity peak corresponding to a Te$_2$ column, with the Mo column sitting directly between the Se and Se$_2$ histogram peaks. It is important to note that here we do not attempt to label individual Te columns, due to the similarity in Z-contrast with the most common chalcogenide configuration, an Se$_2$ column. Given the small number of individual Se atoms, there are likely very few single Te columns in this monolayer region, but they would be included in the Se$_2$ peak.

Finally, we can use the atom labeling to provide a quantitative measurement of the Te doping concentration. Figure 3d shows the histogram of B site HAADF intensities broken up by the configuration each site is most likely to possess based off of its Z-contrast. The image possesses a total of 332 sites, with 18 vacancy sites resulting in a total of 646 atoms, with the 36 Te$_2$ sites and 86 SeTe sites corresponding to a total of 158 Te atoms and a Te doping concentration of ~25%, close to the estimated value of 28% in the alloy B samples (see the Supporting Information). Furthermore, by labeling each atom in the A/B site sorted image by its Z-contrast, we can see the different sites are spread uniformly throughout the area indicating that the sample is completely alloyed (Figure 3e). The 2H symmetry of the alloys at monolayer thickness has been directly imaged and is consistent with previous reports via MBE synthesis due to the stabilizing role of selenium in subduing the 1T′ phase of MoTe$_2$.[41]

In order to understand the preference for complete alloying in these crystals, we calculate the free energies of formation of three MoSe$_{2(1-x)}$Te$_{2x}$ structures: 1, fully alloyed 2H crystals containing Se$_2$, Se−Te and Te$_2$ sites in the anion sublattice as

described previously; 2, partially alloyed 2H crystals containing randomly distributed Se_2 and Te_2 sites, but no Se–Te sites; and 3, phase-separated heterostructures containing $MoSe_2$ and $MoTe_2$ regions separated by a low-energy α boundary along the zigzag direction (depicted in Figure 4).
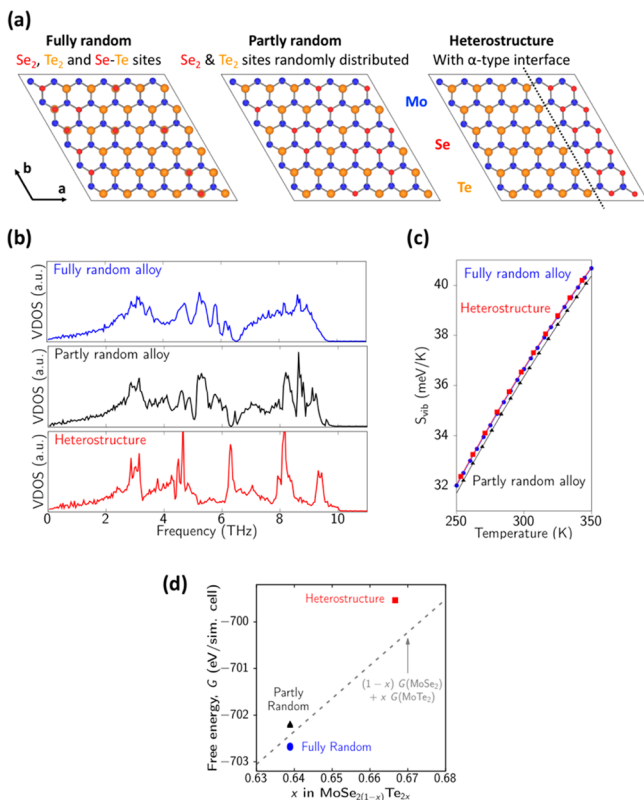

Figure 4. Density functional theory (DFT) simulations of $MoSe_{2(1-x)}Te_{2x}$: (a) three configurations of $MoSe_{2(1-x)}Te_{2x}$ crystals considered in this study including fully and partly random alloys and phase-separated heterostructures; (b) vibrational density of states of the three configurations obtained from empirical MD simulations; (c) calculated vibrational entropies of the fully and partly random alloys and the heterostructure in an infinitely large crystal lying within 0.5 meV of each other at room temperature; (d) calculated free energies of the three structures plotted relative to the linear interpolation between the free energies of the pure $MoSe_2$ and $MoTe_2$ crystals.

The free energy of formation of the three $MoSe_{2(1-x)}Te_{2x}$ structures is defined as

$$\Delta G_f = \Delta U(MoSe_{2(1-x)}Te_{2x}) + \Delta G_{config}(MoSe_{2(1-x)}Te_{2x})$$
$$+ \Delta G_{vib}(MoSe_{2(1-x)}Te_{2x})$$

Hence,

$$\Delta G_f = U(MoSe_{2(1-x)}Te_{2x}) - (1-x)U(MoSe_2) - xU(MoTe_2)$$
$$- T[S_{config}(MoSe_{2(1-x)}Te_{2x}) - (1-x)S_{config}(MoSe_2)$$
$$- xS_{config}(MoTe_2)] - T[S_{vib}(MoSe_{2(1-x)}Te_{2x})$$
$$- (1-x)S_{vib}(MoSe_2) - xS_{vib}(MoTe_2)]$$

where T is the temperature.

The free energy of crystals, G_f, has three components—the internal energy of crystal, U; the configurational free energy, G_{config}; and the vibrational free energy, G_{vib}. The internal energy

of the crystal is taken to be equal to the ground-state energy of the fully relaxed crystal in DFT simulations. The extensive configurational entropy is calculated analytically by enumerating the phase space of $MoSe_{2(1-x)}Te_{2x}$ structures possible in the 108-atoms simulation cell. For example,

$$S_{config} = k_B \ln \Omega$$

where Ω is the number of $MoSe_{2(1-x)}Te_{2x}$ configurations. For a fully random alloy, $S_{config} = k_B \ln \binom{72}{26} = 44.76k_B$, and for a partially random alloy, $S_{config} = k_B \ln \binom{36}{13} = 21.56k_B$.

The vibrational free energy of all structures in this study is computed by integrating the product of temperature-dependent lattice specific heat, $C_V(T)$, with $1/T$. The lattice heat capacity is, in turn, evaluated as the integral of the density of vibrational states with the Bose–Einstein distribution. Phonon density of states are calculated as the Fourier transform of the autocorrelation function of atomic velocities in an equilibrium MD simulation of each $MoSe_{2(1-x)}Te_{2x}$ configuration. The general methodology to compute vibrational properties and specific heat values from MD simulations is described by Vashishta et al.[43]

SI Table 1 shows the calculated internal energy, and configurational and vibrational entropies of $MoSe_{2(1-x)}Te_{2x}$ and $MoSe_2$ and $MoTe_2$ crystals. The calculated free energies of formation of each structure at room temperature, $T = 300$ K, representative of experimental observations, indicate that the fully alloyed $MoSe_{2(1-x)}Te_{2x}$ has the lowest free energy of formation and is thus most thermodynamically stable, consistent with our atomic-resolution STEM-HAADF observations.

In order to understand the interplay between the Se and Te alloyed phases, the samples were investigated with polarized Raman spectroscopy. The setup consisted of adding a half-wave plate and a polarizer in the beam path. As seen in Figure 1b, the Raman spectra of all samples feature a strong peak due the A_{1g} mode starting at ~239 cm^{-1} in the pure $MoSe_2$ sample that successively red shifts. Since the A_{1g} mode features the symmetric out-of-plane breathing of the chalcogen atoms with the central transition metal atom layer stationary, it is sensitive to the polarization of the exciting laser beam. As a result, the A_{1g} peak is absent in the cross-polarized spectrum of pure $MoSe_2$ (Figure 5a).[44] In the case of alloy A, the polarized Raman spectrum in Figure 5b shows a stronger hump at ~285 cm^{-1} due to the E^1_{2g} contribution from $MoSe_2$ as it is the dominant content of that sample. For alloy B, we see a residual hump in the polarized spectrum (olive) at the approximate location of the A_{1g} mode of the unpolarized spectrum (magenta). Given that this mode is observably asymmetric in the case of alloy B, the unpolarized Raman spectrum is deconvoluted and shown in Figure 5d. We see six peaks at 147, 183, 226, 231, 275, and 289 cm^{-1}, respectively. The deconvolution of the strongest mode reveals a primary peak at 231 cm^{-1} and a secondary one at 226 cm^{-1}. The 231 cm^{-1} mode is due to A_{1g} vibration of Se–Mo–Te (but red-shifted due to increased bonding between the common Mo atoms and Te atoms). The 226 cm^{-1} mode is due to the E_{2g} vibration of 2H Te–Mo–Te but similarly red-shifted.[33] This is consistent with the Te atoms alloying with Se atoms in the chalcogen layers. The other modes shown in the figure are E^1_{2g} – LA (M) of 2H $MoSe_2$ (147 cm^{-1}) and A_{1g} of 2H Te–Mo–Te (183 cm^{-1}). The two other modes (275 and 288 cm^{-1}) are most likely due to splitting of E_{2g} (TO+LO) mode of 2H Se–Mo–Se.[45] Therefore, the polarized spectrum of alloy B in Figure 5c
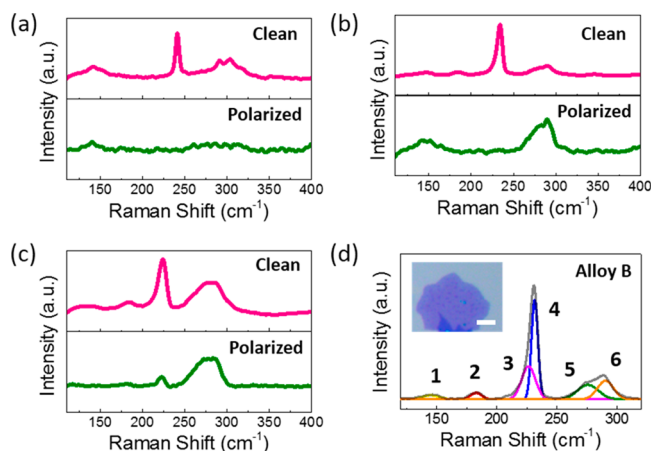
Figure 5. Polarized Raman spectra of $MoSe_{2(1-x)}Te_{2x}$ monolayers: (a–c) clean (magenta) and polarized (olive) Raman spectra of the pure $MoSe_2$ and the alloy samples (in all samples, the strong and fully symmetric A_{1g} mode arising from $MoSe_2$ is precluded due to the symmetry selection rules); (d) deconvoluted clean Raman spectrum of alloy B containing six peaks. The polarized spectrum in panel c contains predominantly peaks 3, 5, and 6 attributed to the E^1_{2g} modes of $MoSe_2$ and $MoTe_2$ (inset optical image scale bar = 5 μm).

can now be understood as consisting predominantly of the E^1_{2g} mode due to Te−Mo−Te atoms and Se−Mo−Se vibrations, respectively. The A_{1g} modes from Te−Mo−Te and Se−Mo−Se are precluded due to the cross-polarization. Thus, the polarized spectra confirm the presence of Se and Te chalcogens in the alloy samples, in consistency with the theoretical calculations and the rest of the experimental results.

In conclusion, we provide an inclusive report of in situ alloying in monolayer $MoSe_{2(1-x)}Te_{2x}$ with increased tellurium content from a facile single-step CVD synthesis via conventional chemical precursors. The alloys show progressive changes in their 2D morphology, Raman and PL spectra corresponding with the tellurium concentration. AFM and XPS analysis reveals the intricate morphological differences and chemical binding energies of the atoms. The atomic-resolution images show that the Te atoms incorporate into the $MoSe_2$ lattice in a stable 2H symmetry. Simulations confirm the thermodynamic phase mixing of the two chalcogens in the monolayer lattice. Finally, comparison of the polarized and unpolarized Raman spectra shows the interplay and coexistence of Se and Te atoms in the chalcogen layers of the CVD-grown monolayer alloys. The work paves the way for understanding doping induced structural changes in interesting 2D materials, i.e., layered systems in the atomically thin limit.

■ EXPERIMENTAL DETAILS

Synthesis. The monolayer $MoSe_{2(1-x)}Te_{2x}$ alloy samples were grown via chemical vapor deposition. The strategy involved synthesizing monolayer $MoSe_2$ via CVD by steadily incorporating tellurium in the 2D structure. According to the relative increasing (decreasing) concentration of tellurium (selenium) precursors, it is convenient to label the samples as "pure $MoSe_2$" and alloys "A" (Se:Te ratio by weight = 1:1) and "B" (Se:Te ratio by weight = 1:5), respectively; this convention is followed henceforth. The pure $MoSe_2$ and Alloy A samples were grown via conventional method inside a 2 in. quartz tube with MoO_3 (center of heating zone) Te (upstream of MoO_3) and Se (upstream of Te) powders in individual porcelain boats as the respective precursors. All powders were obtained from Sigma-Aldrich (99.99%). The SiO_2/Si substrates (precleaned with acetone and isopropanol) were placed face-up downstream of the MoO_3 boat. The

temperature of MoO_3 was increased to 700 °C (temperatures of Te and Se boats were approximately 450 and 200 °C, respectively) and held for 20 min before cooling to ambient temperature. For growing alloy B, a dilute solution of sodium cholate and ammonium molybdate (both obtained from Sigma-Aldrich, 99.99%) in H_2O was spin-coated and drop-casted (respectively) on SiO_2/Si substrates as reported previously.[46] These substrates were placed in a porcelain boat in the center of a 2 in. quartz tube mounted in a tube furnace. The selenium and tellurium powders were uniformly mixed in the aforementioned ratio and placed in a separate porcelain boat upstream of the Mo-coated substrates. High-purity Ar/H_2 (15%) gas was flown throughout the process with the temperature of the target substrates ramped to 700 °C and held for 20 min before cooling to ambient temperature. The monolayer flakes were obtained on the top surface of the substrates.

Characterization. Raman and PL spectra were collected on a Renishaw inVia Raman microscope through a 50× objective lens and 532 nm (unless stated otherwise in the main text) laser. XPS spectra were obtained on a PHI Quantera II SXM machine using Al Kα X-ray source at 1486.6 eV and 26 eV pass energy. HAADF-STEM images were recorded on a Nion aberration-corrected UltraSTEM 100 at an accelerating voltage of 60 kV. The HAADF image was smoothed with a 1 pixel Gaussian blur, and the peak_local_max function available in the sci-kit learn Python library was used to identify the atom positions. Effective Z-contrasts of two atom sites were determined by adding Z values of the constituent atoms in quadrature.

Simulations. The free energies of alloyed and phase-separated $MoSe_{2(1-x)}Te_{2x}$ monolayers were quantified using a combination of DFT and empirical MD simulations. DFT simulations for the calculation of ground-state energies were performed on monolayer $MoSe_{2(1-x)}Te_{2x}$ crystals containing 36 Mo ions and 72 chalcogen (Se or Te) ions, respectively. Spin-polarized DFT simulations were performed with the PBE form of the GGA functional implemented in the VASP program.[47−49] Wave functions were described using a large basis set containing components up to 450 eV. The $MoSe_{2(1-x)}Te_{2x}$ monolayer is relaxed until forces on all ions in the system are below 0.05 eV/A and all components of the residual stress tensor are less than 0.2 GPa.

Vibrational contributions to the free energies of $MoSe_{2(1-x)}Te_{2x}$ structures were estimated from a calculation of the lattice specific heat, which represents the temperature-dependent change of vibrational enthalpy of the system. Specific heat values were calculated from MD simulations of the $MoSe_{2(1-x)}Te_{2x}$ crystals of size 400 Å × 400 Å containing 51972 atoms equilibrated at 300 K for 100 ps in the NVT ensemble. These empirical MD simulations were performed using the LAMMPS molecular dynamics program with interatomic interactions between the Mo, Se, and Te atoms described by classical force fields of the Stillinger−Weber functional form parametrized to reproduce vibrational properties and lattice and elastic constants.[50] Further details about the parametrization of the force field used in this study can be found in section 1 of the Supporting Information.

■ ASSOCIATED CONTENT

Ⓢ Supporting Information

The Supporting Information is available free of charge on the ACS Publications website at DOI: 10.1021/acs.chemmater.8b03444.

   Estimation of chalcogen alloy compositions, stability of samples at ambient conditions, and additional simulation details (PDF)

■ AUTHOR INFORMATION

Corresponding Authors

*(P.V.) E-mail: priyav@usc.edu.
*(C.S.T.) E-mail: cst.iisc@gmail.com.
*(P.M.A.) E-mail: ajayan@rice.edu.

ORCID Ⓘ

Aravind Krishnamoorthy: 0000-0001-6778-2471
Jordan Adam Hachtel: 0000-0002-9728-0920

Aiichiro Nakano: 0000-0003-3228-3896
Priya Vashishta: 0000-0003-4683-429X
Chandra Sekhar Tiwary: 0000-0001-9760-9768

■ **REFERENCES**

(1) Wang, Q. H.; Kalantar-Zadeh, K.; Kis, A.; Coleman, J. N.; Strano, M. S. Electronics and Optoelectronics of Two-Dimensional Transition Metal Dichalcogenides. *Nat. Nanotechnol.* **2012**, *7*, 699−712.

(2) Wang, X.; Gong, Y.; Shi, G.; Chow, W. L.; Keyshar, K.; Ye, G.; Vajtai, R.; Lou, J.; Liu, Z.; Ringe, E.; et al. Chemical Vapor Deposition Growth of Crystalline Monolayer MoSe2. *ACS Nano* **2014**, *8*, 5125−5131.

(3) Mak, K. F.; Lee, C.; Hone, J.; Shan, J.; Heinz, T. F. Atomically Thin MoS2: A New Direct-Gap Semiconductor. *Phys. Rev. Lett.* **2010**, *105*, 136805.

(4) Liu, B.; Fathi, M.; Chen, L.; Abbas, A.; Ma, Y.; Zhou, C. Chemical Vapor Deposition Growth of Monolayer WSe2 with Tunable Device Characteristics and Growth Mechanism Study. *ACS Nano* **2015**, *9*, 6119−6127.

(5) Gao, Y.; Liu, Z.; Sun, D.-M.; Huang, L.; Ma, L.-P.; Yin, L.-C.; Ma, T.; Zhang, Z.; Ma, X.-L.; Peng, L.-M.; Cheng, H.-M.; Ren, W. Large-Area Synthesis of High-Quality and Uniform Monolayer WS2 on Reusable Au Foils. *Nat. Commun.* **2015**, *6*, 8569.

(6) Keyshar, K.; Gong, Y.; Ye, G.; Brunetto, G.; Zhou, W.; Cole, D. P.; Hackenberg, K.; He, Y.; Machado, L.; Kabbani, M.; et al. Chemical Vapor Deposition of Monolayer Rhenium Disulfide (ReS₂). *Adv. Mater.* **2015**, *27*, 4640−4648.

(7) Fu, W.; Chen, Y.; Lin, J.; Wang, X.; Zeng, Q.; Zhou, J.; Zheng, L.; Wang, H.; He, Y.; He, H.; et al. Controlled Synthesis of Atomically Thin 1T-TaS2 for Tunable Charge Density Wave Phase Transitions. *Chem. Mater.* **2016**, *28*, 7613−7618.

(8) Jing, Y.; Zhou, Z.; Cabrera, C. R.; Chen, Z. Metallic VS2Monolayer: A Promising 2D Anode Material for Lithium Ion Batteries. *J. Phys. Chem. C* **2013**, *117*, 25409−25413.

(9) Zhao, S.; Hotta, T.; Koretsune, T.; Watanabe, K.; Taniguchi, T.; Sugawara, K.; Takahashi, T.; Shinohara, H.; Kitaura, R. Two-Dimensional Metallic NbS ₂: Growth, Optical Identification and Transport Properties. *2D Mater.* **2016**, *3*, 025027.

(10) Su, S.-H.; Hsu, Y.-T.; Chang, Y.-H.; Chiu, M.-H.; Hsu, C.-L.; Hsu, W.-T.; Chang, W.-H.; He, J.-H.; Li, L.-J. Band Gap-Tunable Molybdenum Sulfide Selenide Monolayer Alloy. *Small* **2014**, *10*, 2589−2594.

(11) Tedstone, A. A.; Lewis, D. J.; O'Brien, P. Synthesis, Properties, and Applications of Transition Metal-Doped Layered Transition Metal Dichalcogenides. *Chem. Mater.* **2016**, *28*, 1965−1974.

(12) Gao, J.; Kim, Y. D.; Liang, L.; Idrobo, J. C.; Chow, P.; Tan, J.; Li, B.; Li, L.; Sumpter, B. G.; Lu, T.-M.; et al. Transition-Metal Substitution Doping in Synthetic Atomically Thin Semiconductors. *Adv. Mater.* **2016**, *28*, 9735−9743.

(13) Duerloo, K.-A. N.; Reed, E. J. Structural Phase Transitions by Design in Monolayer Alloys. *ACS Nano* **2016**, *10*, 289−297.

(14) Voiry, D.; Mohite, A.; Chhowalla, M. Phase Engineering of Transition Metal Dichalcogenides. *Chem. Soc. Rev.* **2015**, *44*, 2702−2712.

(15) Kochat, V.; Apte, A.; Hachtel, J. A.; Kumazoe, H.; Krishnamoorthy, A.; Susarla, S.; Idrobo, J. C.; Shimojo, F.; Vashishta, P.; Kalia, R.; et al. Re Doping in 2D Transition Metal Dichalcogenides as a New Route to Tailor Structural Phases and Induced Magnetism. *Adv. Mater.* **2017**, *29*, 1703754.

(16) Susarla, S.; Kutana, A.; Hachtel, J. A.; Kochat, V.; Apte, A.; Vajtai, R.; Idrobo, J. C.; Yakobson, B. I.; Tiwary, C. S.; Ajayan, P. M. Quaternary 2D Transition Metal Dichalcogenides (TMDs) with Tunable Bandgap. *Adv. Mater.* **2017**, *29*, 1702457.

(17) Wang, G.; Robert, C.; Suslu, A.; Chen, B.; Yang, S.; Alamdari, S.; Gerber, I. C.; Amand, T.; Marie, X.; Tongay, S.; Urbaszek, B. Spin-Orbit Engineering in Transition Metal Dichalcogenide Alloy Monolayers. *Nat. Commun.* **2015**, *6*, 10110.

(18) Komsa, H.-P.; Krasheninnikov, A. V. Two-Dimensional Transition Metal Dichalcogenide Alloys: Stability and Electronic Properties. *J. Phys. Chem. Lett.* **2012**, *3*, 3652−3656.

(19) Kang, J.; Tongay, S.; Li, J.; Wu, J. Monolayer Semiconducting Transition Metal Dichalcogenide Alloys: Stability and Band Bowing. *J. Appl. Phys.* **2013**, *113*, 143703.

(20) Lin, Y.; Dumcenco, D. O.; Komsa, H.-P.; Niimi, Y.; Krasheninnikov, A. V.; Huang, Y.-S.; Suenaga, K. Properties of Individual Dopant Atoms in Single-Layer MoS2: Atomic Structure, Migration, and Enhanced Reactivity. *Adv. Mater.* **2014**, *26*, 2857−2861.

(21) Dolui, K.; Rungger, I.; Das Pemmaraju, C.; Sanvito, S. Possible Doping Strategies for MoS${}_{2}$ Monolayers: An Ab Initio Study. *Phys. Rev. B: Condens. Matter Mater. Phys.* **2013**, *88*, 075420.

(22) Suh, J.; Park, T.-E.; Lin, D.-Y.; Fu, D.; Park, J.; Jung, H. J.; Chen, Y.; Ko, C.; Jang, C.; Sun, Y.; et al. Doping against the Native Propensity of MoS2: Degenerate Hole Doping by Cation Substitution. *Nano Lett.* **2014**, *14*, 6976−6982.

(23) Laskar, M. R.; Nath, D. N.; Ma, L.; Lee, E. W.; Lee, C. H.; Kent, T.; Yang, Z.; Mishra, R.; Roldan, M. A.; Idrobo, J.-C.; et al. p-Type Doping of MoS2 Thin Films Using Nb. *Appl. Phys. Lett.* **2014**, *104*, 092104.

(24) Das, S.; Demarteau, M.; Roelofs, A. Nb-Doped Single Crystalline MoS2 Field Effect Transistor. *Appl. Phys. Lett.* **2015**, *106*, 173506.

(25) Zhang, K.; Feng, S.; Wang, J.; Azcatl, A.; Lu, N.; Addou, R.; Wang, N.; Zhou, C.; Lerach, J.; Bojan, V.; et al. Manganese Doping of Monolayer MoS2: The Substrate Is Critical. *Nano Lett.* **2015**, *15*, 6586−6591.

(26) Sigiro, M.; Huang, Y.-S.; Ho, C.-H.; Lin, Y.-C.; Suenaga, K. Influence of Rhenium on the Structural and Optical Properties of Molybdenum Disulfide. *Jpn. J. Appl. Phys.* **2015**, *54*, 04DH05.

(27) Gong, Y.; Liu, Z.; Lupini, A. R.; Shi, G.; Lin, J.; Najmaei, S.; Lin, Z.; Elías, A. L.; Berkdemir, A.; You, G.; et al. Band Gap Engineering and Layer-by-Layer Mapping of Selenium-Doped Molybdenum Disulfide. *Nano Lett.* **2014**, *14*, 442−449.

(28) Yu, P.; Lin, J.; Sun, L.; Le, Q. L.; Yu, X.; Gao, G.; Hsu, C.-H.; Wu, D.; Chang, T.-R.; Zeng, Q.; et al. Metal−Semiconductor Phase-Transition in WSe2(1-x)Te2x Monolayer. *Adv. Mater.* **2017**, *29*, 1603991.

(29) Zhou, L.; Xu, K.; Zubair, A.; Liao, A. D.; Fang, W.; Ouyang, F.; Lee, Y. H.; Ueno, K.; Saito, R.; Palacios, T.; Kong, J.; Dresselhaus, M. S. Large-Area Synthesis of High-Quality Uniform Few-Layer MoTe₂. *J. Am. Chem. Soc.* **2015**, *137*, 11892−11895.

(30) Naylor, C. H.; Parkin, W. M.; Ping, J.; Gao, Z.; Zhou, Y. R.; Kim, Y.; Streller, F.; Carpick, R. W.; Rappe, A. M.; Drndic, M.; et al. Monolayer Single-Crystal 1T′-MoTe2 Grown by Chemical Vapor Deposition Exhibits a Weak Antilocalization Effect. *Nano Lett.* **2016**, *16*, 4297−4304.

(31) Torun, E.; Sahin, H.; Cahangirov, S.; Rubio, A.; Peeters, F. M. Anisotropic Electronic, Mechanical, and Optical Properties of Monolayer WTe2. *J. Appl. Phys.* **2016**, *119*, 074307.

(32) Jiang, J.; Liu, Z. K.; Sun, Y.; Yang, H. F.; Rajamathi, C. R.; Qi, Y. P.; Yang, L. X.; Chen, C.; Peng, H.; Hwang, C.-C.; et al. Signature of Type-II Weyl Semimetal Phase in MoTe2. *Nat. Commun.* **2017**, *8*, 13973.

(33) Keum, D. H.; Cho, S.; Kim, J. H.; Choe, D.-H.; Sung, H.-J.; Kan, M.; Kang, H.; Hwang, J.-Y.; Kim, S. W.; Yang, H.; et al. Bandgap Opening in Few-Layered Monoclinic MoTe2. *Nat. Phys.* **2015**, *11*, 482−486.

(34) Song, S.; et al. Room Temperature Semiconductor-Metal Transition of MoTe2 Thin Films Engineered by Strain. *Nano Lett.* **2016**, *16*, 188−193.

(35) Ali, M. N.; Xiong, J.; Flynn, S.; Tao, J.; Gibson, Q. D.; Schoop, L. M.; Liang, T.; Haldolaarachchige, N.; Hirschberger, M.; Ong, N. P.; et al. Large, Non-Saturating Magnetoresistance in WTe2. *Nature* **2014**, *514*, 205−208.

(36) Zhang, E.; Chen, R.; Huang, C.; Yu, J.; Zhang, K.; Wang, W.; Liu, S.; Ling, J.; Wan, X.; Lu, H.-Z.; et al. Tunable Positive to Negative Magnetoresistance in Atomically Thin WTe2. *Nano Lett.* **2017**, *17*, 878−885.

(37) Tang, S.; Zhang, C.; Wong, D.; Pedramrazi, Z.; Tsai, H.-Z.; Jia, C.; Moritz, B.; Claassen, M.; Ryu, H.; Kahn, S.; et al. Quantum Spin Hall State in Monolayer 1T′-WTe2. *Nat. Phys.* **2017**, *13*, 683−687.

(38) Sung, J. H.; Heo, H.; Si, S.; Kim, Y. H.; Noh, H. R.; Song, K.; Kim, J.; Lee, C.-S.; Seo, S.-Y.; Kim, D.-H.; et al. Coplanar Semiconductor−Metal Circuitry Defined on Few-Layer MoTe2 via Polymorphic Heteroepitaxy. *Nat. Nanotechnol.* **2017**, *12*, 1064−1070.

(39) Wang, Y.; Xiao, J.; Zhu, H.; Li, Y.; Alsaid, Y.; Fong, K. Y.; Zhou, Y.; Wang, S.; Shi, W.; Wang, Y.; et al. Structural Phase Transition in Monolayer MoTe2 Driven by Electrostatic Doping. *Nature* **2017**, *550*, 487−491.

(40) Zhang, C.; KC, S.; Nie, Y.; Liang, C.; Vandenberghe, W. G.; Longo, R. C.; Zheng, Y.; Kong, F.; Hong, S.; Wallace, R. M.; et al. Charge Mediated Reversible Metal−Insulator Transition in Monolayer MoTe2 and WxMo1−XTe2 Alloy. *ACS Nano* **2016**, *10*, 7370−7375.

(41) Diaz, H. C.; Ma, Y.; Kolekar, S.; Avila, J.; Chen, C.; Asensio, M. C.; Batzill, M. Substrate Dependent Electronic Structure Variations of van Der Waals Heterostructures of MoSe$_2$ or MoSe$_{2(1−x)}$Te$_{2x}$ Grown by van Der Waals Epitaxy. *2D Mater.* **2017**, *4*, 025094.

(42) Lin, J.; Zhou, J.; Zuluaga, S.; Yu, P.; Gu, M.; Liu, Z.; Pantelides, S. T.; Suenaga, K. Anisotropic Ordering in 1T′ Molybdenum and Tungsten Ditelluride Layers Alloyed with Sulfur and Selenium. *ACS Nano* **2018**, *12*, 894−901.

(43) Vashishta, P.; Kalia, R. K.; Nakano, A.; Rino, J. P. Interaction Potential for Aluminum Nitride: A Molecular Dynamics Study of Mechanical and Thermal Properties of Crystalline and Amorphous Aluminum Nitride. *J. Appl. Phys.* **2011**, *109*, 033514.

(44) Zhao, W.; Ghorannevis, Z.; Amara, K. K.; Pang, J. R.; Toh, M.; Zhang, X.; Kloc, C.; Tan, P. H.; Eda, G. Lattice Dynamics in Mono- and Few-Layer Sheets of WS2 and WSe2. *Nanoscale* **2013**, *5*, 9677−9683.

(45) Molina-Sánchez, A.; Wirtz, L. Phonons in Single-Layer and Few-Layer MoS2 and WS2. *Phys. Rev. B: Condens. Matter Mater. Phys.* **2011**, *84*, 155413.

(46) Chen, S. Y.; Naylor, C. H.; Goldstein, T.; Johnson, A. T. C.; Yan, J. Intrinsic Phonon Bands in High-Quality Monolayer T′ Molybdenum Ditelluride. *ACS Nano* **2017**, *11*, 814−820.

(47) Perdew, J. P.; Burke, K.; Ernzerhof, M. Generalized Gradient Approximation Made Simple. *Phys. Rev. Lett.* **1996**, *77*, 3865−3868.

(48) Kresse, G.; Furthmüller, J. Efficient Iterative Schemes for Ab Initio Total-Energy Calculations Using a Plane-Wave Basis Set. *Phys. Rev. B: Condens. Matter Mater. Phys.* **1996**, *54*, 11169−11186.

(49) Kresse, G.; Furthmüller, J. Efficiency of Ab-Initio Total Energy Calculations for Metals and Semiconductors Using a Plane-Wave Basis Set. *Comput. Mater. Sci.* **1996**, *6*, 15−50.

(50) Plimpton, S. Fast Parallel Algorithms for Short-Range Molecular Dynamics. *J. Comput. Phys.* **1995**, *117*, 1−19.